

High-Resolution Random Mesh Algorithms for Creating a Probabilistic 3D Surface Atlas of the Human Brain

P. M. THOMPSON, C. SCHWARTZ, AND A. W. TOGA

Laboratory of Neuro Imaging, Department of Neurology, Division of Brain Mapping, UCLA School of Medicine, Los Angeles, California 90095-1769

Received October 29, 1995

Striking variations exist, across individuals, in the internal and external geometry of the brain. Such normal variations in the size, orientation, topology, and geometric complexity of cortical and subcortical structures have complicated the problem of quantifying deviations from normal anatomy and of developing standardized neuroanatomical atlases. This paper describes the design, implementation, and results of a technique for creating a three-dimensional (3D) probabilistic surface atlas of the human brain. We have developed, implemented, and tested a new 3D statistical method for assessing structural variations in a database of anatomic images. The algorithm enables the internal surface anatomy of new subjects to be analyzed at an extremely local level. The goal was to quantify subtle and distributed patterns of deviation from normal anatomy by automatically generating detailed probability maps of the anatomy of new subjects. Connected systems of parametric meshes were used to model the internal course of the following structures in both hemispheres: the parieto-occipital sulcus, the anterior and posterior rami of the calcarine sulcus, the cingulate and marginal sulci, and the supracallosal sulcus. These sulci penetrate sufficiently deeply into the brain to introduce an obvious topological decomposition of its volume architecture. A family of surface maps was constructed, encoding statistical properties of local anatomical variation within individual sulci. A probability space of random transformations, based on the theory of Gaussian random fields, was developed to reflect the observed variability in stereotaxic space of the connected system of anatomic surfaces. A complete system of probability density functions was computed, yielding confidence limits on surface variation. The ultimate goal of brain mapping is to provide a framework for integrating functional and anatomical data across many subjects and modalities. This task requires precise quantitative knowledge of the variations in geometry and location of intracerebral structures and critical functional interfaces. The surface mapping and probabilistic techniques presented here provide a basis for

the generation of anatomical templates and expert diagnostic systems which retain quantitative information on intersubject variations in brain architecture. © 1996 Academic Press, Inc.

INTRODUCTION

Dramatic variations exist, across individuals, in the internal and external geometry of the human brain (Sanides, 1962). Accurate clinical diagnosis often requires the severity of deviations from normal anatomy to be quantified precisely. This exercise is especially difficult in the brain because its internal geometry is highly individual in character. In particular, normal variations in the size, orientation, topology, and geometric complexity of cortical and subcortical structures have complicated the goals of comparing functional and anatomic data from many subjects and of developing standardized atlases of the human brain.

The quantitative comparison of brain architecture across different subjects requires a common coordinate system, with respect to which the spatial variability of features from different individuals can be expressed (Evans *et al.*, 1996). Stereotaxic localization, for example, provides a quantitative system of reference in human functional studies and stereotaxic surgical procedures. While stereotaxic atlases supply a common reference coordinate system, their usefulness ultimately depends on how closely the scans of individual subjects match the representation of anatomy provided by the atlas. Anatomic correspondence is especially critical at functional interfaces and cytoarchitectonic boundaries, such as those framed by the deep internal banks of primary sulci (Rademacher *et al.*, 1993). The inherent neuroanatomic variability between individuals, as well as the numerous differences between stereotaxic systems themselves (Burzaco, 1985), warrants the development of a well-defined reference system able to represent and classify idiosyncratic, age-related, developmental, or pathologic variations in anatomy.

A digital anatomic atlas of the human brain, incorporating precise statistical information on positional and geometric variability of important functional and anatomic interfaces, presents a likely solution (Mazziotta *et al.*, 1995). In particular, an atlas incorporating the concept of confidence limits, rather than an absolute representation of anatomy, may be more appropriate to represent any given subpopulation.

Probabilistic Atlases

The surface-based approach presented in this paper enables the internal surface anatomy of new subjects' brains to be analyzed at an extremely local level. Relative to an average representation of neuroanatomy, the anatomy of a new subject will exhibit subtle and distributed patterns of local deviation. The severity of this local deviation is quantified automatically by our algorithm, and the resulting values are displayed in the form of a probability map on a graphical surface model of the anatomy of the subject. Regional patterns of abnormality are then highlighted and color-coded on this 3D surface representation. The resulting surface system may be rotated, magnified, and animated interactively for detailed examination and clinical diagnosis.

Our probability maps are based on a new method for the 3D statistical analysis of anatomic images. A database of anatomic scans from normal individuals is used by the algorithm to quantify local structural variations in their anatomy. In deriving the parameters of anatomic variation, the algorithm accounts for the fact that the magnitude of anatomic variability, as well as its local directional bias, differs significantly at every single point in the anatomy of the brain. Finally, the method presented here is capable of characterizing simultaneously the variations in location and geometry, across different individuals, of multiple, complex, branching, and arbitrarily connected anatomic surfaces in the brain (Thompson *et al.*, 1995, 1996).

An analysis of many brains with subtle and distributed variations in geometry is used to generate a statistical characterization of the region of stereotaxic space in which each particular structure is most likely to be found. Such statistical data define a restricted area or a central reference point (or region) of localization for specific structures, within a standard stereotaxic coordinate system (Hardy, 1994). Ultimately, probability distributions encoding the likelihood of finding a specific structure within certain coordinate ranges of stereotaxic space will result in an atlas general enough to be representative of the entire species. The resultant atlas will be flexible enough to retain, and directly represent, information on the anatomic variability inherent in human subpopulations.

Initial attempts to derive average representations of neuroanatomy have underscored the validity and

power of this approach in both clinical and research settings (Evans *et al.*, 1992; Andreasen *et al.*, 1994). In one such approach, 305 MRI volumes (2-mm-thick slices) were mapped by linear transformation into stereotaxic space, intensity normalized, and averaged on a voxel-by-voxel basis (Evans *et al.*, 1992). The effect of anatomical variability in different brain areas is illustrated qualitatively by this average intensity MRI dataset. Nevertheless, the average brain which results has regions where individual structures are blurred out due to spatial variability in the population, making it insufficient as a quantitative tool (Evans *et al.*, 1992, 1994b).

Our approach to quantifying the geometric variance of anatomic surfaces in the human brain requires a rigorous formulation of probability measures on free-form curves and surfaces in 3D. Connected systems of parametric meshes were used to model the internal course of the following structures in both hemispheres: the parieto-occipital sulcus, the anterior and posterior rami of the calcarine sulcus, the cingulate and marginal sulci, and the supracallosal sulcus. A probability space of random transformations, based on the theory of Gaussian random fields, is developed to reflect the observed variability in stereotaxic space of the connected system of anatomic surfaces.

Prior to the description of the surface mapping algorithms, we briefly review those aspects of the internal surface anatomy and function of the sulci which favored their selection as key components of a probabilistic atlas of the brain.

Sulcal Anatomy and Surface Mapping

Sulci were selected as the basis for structural analysis of the internal surface anatomy of the brain because they separate functionally distinct regions of the brain and provide a natural topographic partition of its anatomy. Whereas functional or architectonic boundaries are not directly visible in MR imaging, these boundaries bear a well-documented and characteristic relation to the banks, depths, secondary branches, and internal points of confluence of the sulci. Moreover, most of the junctional zones between adjacent microanatomic fields run along the beds of major or minor cortical sulci (Sanides, 1962).

Despite their anatomic and functional significance, even the gyri and sulci which consistently appear in all normal subjects exhibit pronounced variability in size and configuration (Bailey and von Bonin, 1951). Ultimately, direct reference to the internal sulcal surfaces that frame architectonic fields may provide additional bases for functional mapping in a 3D coordinate grid (Rademacher *et al.*, 1993; cf. Steinmetz *et al.*, 1990).

Serial sectioning of whole human heads, in conjunction with full-color digital photography of the specimen, offers the highest resolution technique for imag-

ing sulcal anatomy (Toga *et al.*, 1995; cf. Steinmetz *et al.*, 1989, 1990; Vannier *et al.*, 1991). Modern whole-brain physical sectioning (cryosection) procedures regularly generate 1024^2 – 2048^2 pixel resolution, full-color images of contiguous sections 20–50 μm thick (Quinn *et al.*, 1993; Toga *et al.*, 1994a,b, 1995, 1996). In addition, the image depth afforded by 24-bit full-color images provides excellent color pigment differentiation and texture contrast at the exterior surface of the cortical laminae and at gray–white matter interfaces flanking the sulci. Accordingly, high-resolution images of cryosectioned human anatomy offer the spatial and densitometric resolution necessary for accurate quantitative analysis of the internal surface geometry of the human brain.

In order to spatially characterize the morphometric variability in the interior surface geometry of the brain, we modeled the major sulci in 3D as deep internal structures. Their internal surfaces were modeled using a multiresolution parametric mesh approach. As major structural and functional interfaces in the brain, primary sulci are easily identifiable, in both high-resolution cryosection images and lower resolution clinical scans. As well as marking critical gyral and lobar boundaries, the chosen sulci penetrate sufficiently deeply into the brain to form a natural partition of its cellular architecture. Consequently, their internal trajectories are sufficiently extended inside the brain to reflect subtle and distributed variations in neuroanatomy between individuals.

MATERIALS AND METHODS

Cryosectioning and Image Acquisition

The protocol for whole human head cryosectioning and digital image capture was performed as described previously (Quinn *et al.*, 1993; Toga *et al.*, 1994a,b, 1995, 1996). Six normal cadavers (age range 72–91 years, three males) were obtained, optimally within 5–10 hours *post mortem*, through the Willed Body Program at the UCLA School of Medicine. Exclusion criteria were applied to ensure that, in each case, the primary cause of death had not involved any pathologic or traumatic impact on the brain. (The primary causes of death were recorded as follows: pulmonary edema/congestive failure; heart failure; cirrhosis; bacterial pneumonia; respiratory failure, and malignant melanoma. All experimental procedures were conducted in accordance with UCLA Medical Center policies on donor confidentiality and Federal Health and Safety Codes.)

Specimens were prepared for sectioning, in three of the six cases, by perfusing with 8% formalin, cryoprotecting with 10% glycerol, freezing in isopentane and dry ice, and blocking in green tempura paint and 3% sucrose solution. The heads were cryosectioned at

–25°C through the horizontal plane in 50- μm increments, on a heavy-duty cryomacrotome (PMV Stockholm, Sweden). In each case the cranium was left intact in order to preserve the brain's *in situ* conformation and to prevent relaxation of the cerebellum and splaying of the interhemispheric vault (Toga *et al.*, 1994b). The cryomacrotome was equipped with a DigiStat $1024^2 \times 24$ -bit full-color camera (DAGE MTI, Michigan City, IN) for digital image capture of the cryoplaned specimen. Spatial integrity of the data volume was guaranteed by digitizing the 1200–1300 serial images from the specimen blockface itself during the sectioning process (Quinn *et al.*, 1993). This protocol ensures that each consecutive section is in perfect register with its predecessors. In the three remaining cases, the whole nonperfused head was immediately removed and placed on ice and saline, while extraneous soft tissues were removed from the skull. The specimen was frozen *in situ* in isopentane chilled by an external bath of liquid nitrogen. The occipital region of the frozen calvarium was removed with a Stryker bone saw, and the specimen was blocked into freezing distilled water before cryosectioning.

3D Image Reconstruction and Transformation to Stereotaxic Space

Image data from each of the six heads were assigned real-world coordinate values in micrometers for width, height, and depth. Three-dimensional reconstruction of the serial images resulted in a digital data volume that was subsequently transformed into the Talairach stereotaxic coordinate system (Talairach *et al.*, 1967).

A series of steps were required to map each 3D data volume into Talairach space, using the transformations specified in the atlas (Talairach *et al.*, 1967). The locations of the superior margin of the anterior commissure and inferior margin of the posterior commissure were identified and described in pixel coordinates. Piecewise affine transformations were used to vertically align the interhemispheric fissure and transpose the volume to a horizontal origin at the AC–PC line. A complete set of images was then generated for all six heads, by digitally resampling the volume at 500- μm increments in each of the sagittal, coronal, and horizontal planes.

Criteria for Delineating Sulci

After placement of the standardized individual data into the Talairach stereotaxic grid, the complex internal paths of the major deep sulcal fissures in the brain were reconstructed using a contour-based system. With the aid of an interactive contouring program developed in our laboratory, all sulci were outlined manually, according to the detailed anatomic criteria set out in (Steinmetz *et al.*, 1989). Additional formal guidelines were devised and applied when identifying the

exact course of individual sulci in three dimensions (see Fig. 1).

Cellular interfaces between gray and white matter were used to define the opposing banks of the sulci, rather than the more diffuse boundary of gray matter at the external limit of the cortical layer. The high densitometric gradient of the anatomic images at these banks allows them to be identified with single-pixel accuracy. Consequently, the internal path of each sulcus was defined as the medial curve equidistant between the opposing white matter banks on either side. In rare cases, where the white matter was faint, adjacent sections were viewed for additional information. At high magnification, the outline of each sulcus was defined to be the medial axis equidistant from each bank. This contour was traced manually in all the sagittal sections in which it could be distinguished. At the external cerebral surface, the convex hull of the cortex served as an exterior limit.

Sulcal outlines were digitized as a cursor was moved over a highly magnified image of each slice, along the curvilinear path of each sulcus. As a guide to the anatomic relations of the selected sulci, Fig. 2 shows a sagittal projection of all the contours traced in the left hemisphere of one specimen.

Mesh Generation and Surface Reconstruction

Interactive outlining of sulci, as described above, resulted in a sampling of approximately 15,000 points per sulcus. Although this dense system of points captures the details of each sulcal surface at a very local level, their spatial distribution is not quite uniform and

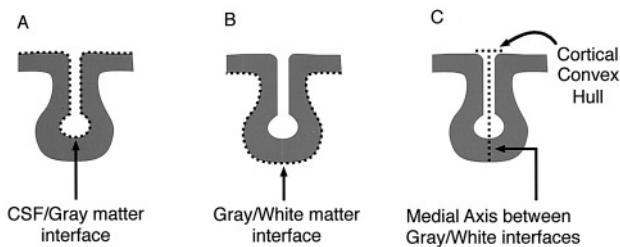


FIG. 1. Rules for delineating sulci. The ability to resolve neuroanatomic boundaries is critical for accurate structure delineation. Three methods are shown for defining the interior course of sulci in cryosection images. The densitometric gradient afforded by 24-bit full-color images provides excellent color pigment differentiation and texture contrast at the exterior surface of the cortical laminae (A) and at gray–white matter interfaces flanking the sulci (B). Nevertheless, a medial axis definition (C), adopted here, provides a fundamental laminar path into the brain for each primary sulcus, whose structural integrity is not compromised in regions where secondary sulci branch away or at points of confluence with other sulci. In addition, method (C) is adaptable for use with other anatomic imaging modalities such as MRI, in which cellular interfaces are blurred out or more diffusely represented. The course of medial axis is not affected by any purely symmetrical errors which occur in identifying the opposing sulcal banks. It can therefore be identified in an accurate and reproducible way, even in low-contrast imaging modalities.

is arbitrarily dependent on how the sagittal sampling planes intersect the sulcus being outlined. To eliminate this dependency, we derived a standard surface representation of the same type, for each sulcus. A parametric grid of 100×150 uniformly spaced points, which act as nodes in a regular rectangular mesh, is stretched over the sulcal surface (Fig. 3). Each resultant surface mesh is analogous in form to a regular rectangular grid, drawn on a rubber sheet, which is subsequently stretched to match all the data points. This scheme provides a means for converting dense systems of points, sampled during outlining, into fully parametric surfaces which can be analyzed, visualized, and compared geometrically and statistically. The mesh construction algorithm can be found in the Appendix. Parameterization of the sulcal outlines from the six specimens resulted in a set of six regular parametric meshes, of identical resolution, for each sulcus, in each hemisphere.

Displacement Maps on Sulcal Surface Meshes

In our formulation, all 60 meshes representing sulcal surfaces were defined on a grid of the same resolution (100×150) so that the relationship between two sulci of the same type could be represented as a map which displaces one surface mesh onto another, in stereotaxic space. For each and every point on a surface mesh M_1 , and every point on a similar mesh M_2 , the two points were matched if they had the same grid location within their respective surfaces. For each such association, the discrepancy was computed as a 3D displacement vector between corresponding nodal points. Ultimately, this procedure yielded a full displacement map for every pair of surfaces of the same type.

Furthermore, an average surface representation was derived for each sulcal type by averaging the 3D position vectors of nodes which correspond, across all six specimens (Fig. 4). This representation also provided a means for quantifying the local variability of internal points in a sulcal surface, on the basis of our sample of parametric surfaces taken from our six specimens. Local measures of spatial variance are based upon the availability of an average surface representation, together with the concept of a *sulcal mapping*, which is a type of displacement map. Briefly, a sulcal mapping is specified by a set of 3D displacement vectors which take each nodal point from its latticial position in the *average* surface mesh onto its corresponding point in a mesh representing the same surface in *another* brain (see Fig. 5; cf. Martin *et al.*, 1994; Sclaroff and Pentland, 1994). Sulcal maps were calculated for all 60 surfaces, relating each one to its respective average surface. Three-dimensional probability distributions were then derived locally from the sulcal maps, according to the mathematical theory which follows.

PROBABILITY MAPPING THEORY

Surface Maps and Statistical Measures

For each sulcus, we now have a family, \mathcal{F} , of n different surface meshes representing that sulcus in n separate individuals, drawn from a specific population. If $\mathbf{r}_i(u,v)$ is the 3D position in stereotaxic space of the point with parametric coordinates (u,v) on the i th mesh, then the average sulcal surface is given by another mesh of the form

$$\mathbf{r}_\mu(u,v) = (1/n) \sum_{i=1 \text{ to } n} \mathbf{r}_i(u,v), \quad \forall (u,v) \in \Omega \quad (\text{Fig. 4}).$$

The variability in stereotaxic position for points internal to a sulcal surface is then given by the scalar variance function $s^2(u,v) = (1/n) \sum_{i=1 \text{ to } n} \|\mathbf{r}_i(u,v) - \mathbf{r}_\mu(u,v)\|^2$, which is defined at each node (u,v) . The square root of this function yields an estimate of the standard deviation in stereotaxic position as a 3D r.m.s. distance for each internal point on the surface. The appropriate numerical value, at each grid point, is given by the root mean square magnitude of the 3D displacement vectors assigned to that point, in the six surface maps from average to specimen. The values of this function are in Talairach mm, and their range can be linearly mapped via a look-up table onto a color range. Profiles of local variability can therefore be visualized, as they vary across each sulcal surface (Fig. 6).

3D Distribution Theory

To make the transition from statistical to probabilistic descriptions of anatomic variation, we derived a complete set of local probability density functions encoding the magnitude and directional biases of local variability within individual sulci.

Consider a general mesh $\mathbf{M} = \{\mathbf{r}(u,v)\}$ selected from the same population as the meshes in the family \mathcal{F} . The discrepancy between the mesh \mathbf{M} and the average mesh $\mathbf{M}_\mu = \{\mathbf{r}_\mu(u,v)\}$ can be represented by the displacement map $\Delta(u,v) = (\mathbf{r}(u,v) - \mathbf{r}_\mu(u,v))$, for all pairs of corresponding grid points $\mathbf{r}(u,v)$ and $\mathbf{r}_\mu(u,v)$. For each (u,v) , the associated displacement maps $\mathbf{d}_i(u,v)$ represent a sample of (vector) observations from a zero mean, spatially anisotropic distribution. The density function of the local distribution, at the mesh point indexed by the coordinates (u,v) , will be denoted by $p(\Delta(u,v))$. Density functions will differ for different nodes, depending on $\Psi_{\mathcal{F}}(u,v)$, the covariance structure of the maps at each individual point. The mathematical form and role of the covariance matrix are described in the Appendix; briefly, its values are used to encode the shape of the dispersion in space of the sulcal node indexed by (u,v) , across a population of individuals. With the exception of 3D nonlinear warping algorithms

(Evans *et al.*, 1991; Miller *et al.*, 1993), which estimate a nonisotropic displacement field matching two 3D brain volumes, few studies have addressed the question of whether the patterns of anatomic variation across individuals are spatially isotropic or whether they display an inherent directional bias. In our formulation, the parametric form of the covariance matrix, $\Psi_{\mathcal{F}}(u,v)$, with its large number of spatial and directional degrees of freedom, enables us to relax the assumption that local variability is isotropic and permits us to calculate directional components conveniently. For each sulcus, probability equations based on anisotropic 3D Gaussian distributions (see Appendix) were used to assign a set of 15,000 different nodal probability density functions which encoded the distribution of general meshes \mathbf{M} around the average representation \mathbf{M}_μ of each sulcus.

3D Confidence Limits for Surface Variability

Confidence limits are commonly used to summarize the inherent dispersion in a probability distribution. Although intervals serve as confidence limits for quantities varying in one dimension, confidence regions are used to summarize the dispersion of higher dimensional quantities such as the variable spatial location of an anatomic point in stereotaxic space. Samples drawn from a multivariate Gaussian population tend to fall in a single cloud or cluster, whose center and shape are determined by the mean vector and covariance matrix of the distribution. A $q\%$ confidence region for the distribution of an anatomic point designates a region of stereotaxic space in which the point is found in $q\%$ of individuals. Equivalently, the chance is $q\%$ of finding the point within the designated region in a randomly selected individual from the same population.

In order to characterize and quantify unusual variations in the anatomy of each sulcus, the ultimate goal is to assign a probability to each node $\mathbf{r}^*(u,v)$ in meshes \mathbf{M}^* representing sulci in new individuals. The numerical value $p_{\mathbf{M}^*}(u,v)$ gives the probability of a sulcal point which is homologous to $\mathbf{r}^*(u,v)$ being even more unusually situated, given the family of similar sulci sampled in the population as a whole. For increasingly extreme deviations, $\Delta^*(u,v)$, of $\mathbf{r}^*(u,v)$ from the average representation of sulcal anatomy, the probability of finding a similar point as far out will be correspondingly lower.

If we let $\chi^2_{3df}(\alpha)$ denote the critical value of the χ^2 distribution (with 3 degrees of freedom) such that $\Pr\{\chi^2_{3df} \geq \chi^2_{3df}(\alpha)\} = \alpha$, then, as we prove mathematically in the Appendix, the $100(1 - \alpha)\%$ confidence region for the stereotaxic position of the surface node at (u,v) is given in implicit form by the equation

$$\Pr\{[\Delta^*(u,v)]^T [\Psi_{\mathcal{F}}(u,v)]^{-1} [\Delta^*(u,v)] \leq \chi^2_{3df}(\alpha)\} = 1 - \alpha.$$

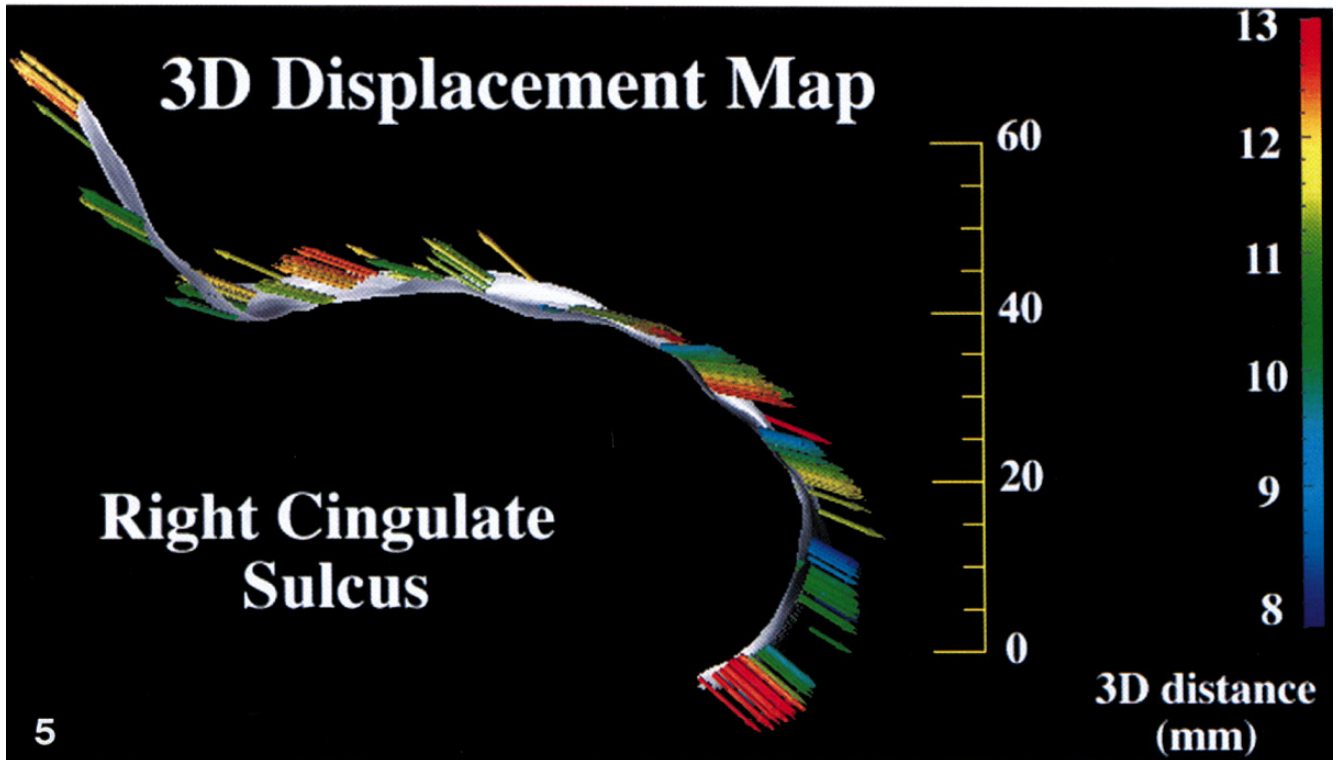
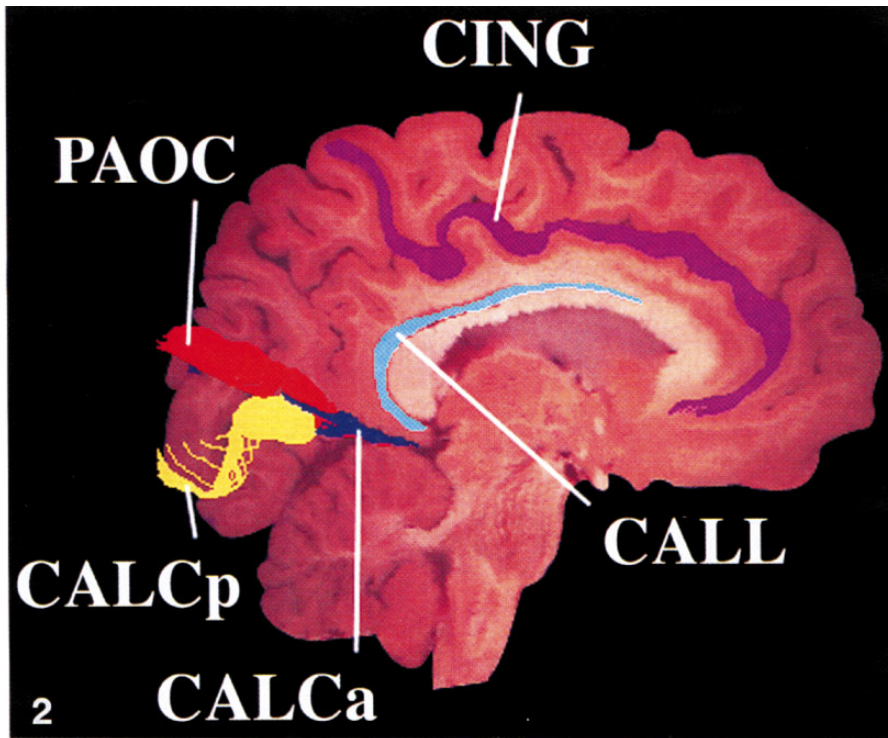


FIG. 2. Sagittal projection of the full set of sulcal contours traced in the left hemisphere of a single brain. These sets of contours were derived from the full series of sectional images spanning the left hemisphere of one brain specimen. Orthogonally projected contours of the anterior and posterior rami of the calcarine sulcus (CALCa and CALCp), as well as the cingulate (CING), supracallosal (CALL) and parieto-occipital (PAOC) sulci, are shown overlaid on one representative sagittal section.

FIG. 5. A 3D displacement map shown on a 3D representation of the right cingulate sulcus. Local discrepancies between individual sulci and their respective average surface can readily be calculated. Both the magnitude and the direction of such surface discrepancies are

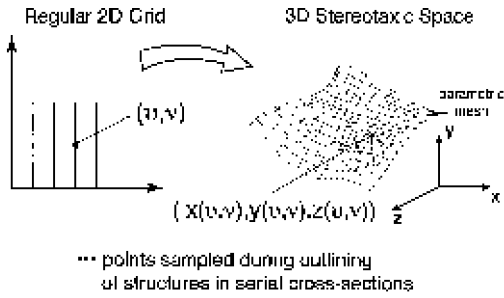


FIG. 3. Parametric mesh construction. The outlining process generates a densely sampled set of points which are known to be located on the internal surface of a sulcus (indicated by isolated points, above right). These points, however, are not distributed uniformly on the sulcal surface. The primary problem with 3D surface statistics is finding homologous points on different surfaces. Homologous point isolation involves the molding of a lattice-like mesh onto the geometric profile of the surface, so that each point on the mesh can be averaged with its counterparts on other surfaces. The concept is similar to that of a regular net being stretched over an object. The imposition of an identical regular structure on surfaces from different specimens allows surface statistics to be derived. Local statistical comparisons are then made by associating points with identical grid locations within their respective surfaces. Points on each surface with the same mesh coordinate occupy similar positions in relation to the geometry of the surface they belong to and are therefore regarded as homologous.

In other words, in a randomly selected individual from the population being considered, the probability is $(1 - \alpha)$ that the sulcal point $\mathbf{r}(u, v)$ will fall inside an ellipsoid defined mathematically by the equation $\mathbf{x}^T[\Psi_{\mathcal{F}}(u, v)]^{-1}\mathbf{x} = \chi^2_{3df}(\alpha)$, and centered around the point $\mathbf{r}_{\mu}(u, v)$ on the average mesh for the sulcus in question. Confidence regions for each surface node are therefore defined by a series of nested ellipsoids in displacement space, the associated threshold probabilities being given by the total density outside each respective confidence region.

Probabilistic Analysis of Surface Anatomy in New Subjects

So far we have constructed a complete set of local probability density functions encoding the likelihood of arbitrary vector discrepancies between a sulcus in a randomly selected subject and the average representation of the same sulcus. For each sulcal type, we have a family $\mathcal{F} = \{\mathbf{M}_i, \Omega, n\}$ of parametric meshes representing the sulcus in n different individuals. (Here we use ω to represent the set of values which may be taken by (u, v) , the two parameters used to index the grid points of each mesh). We also have a set of $I \times J$ nodal probability density functions for a densely sampled set of

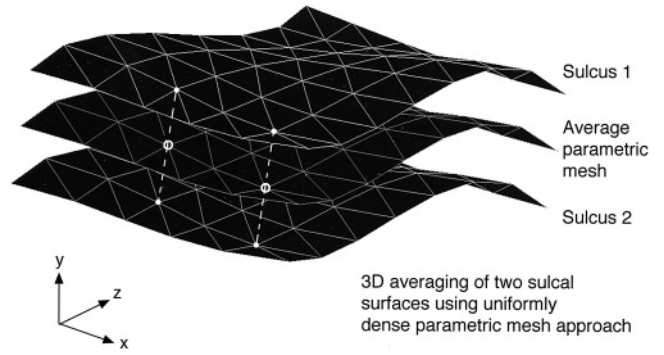


FIG. 4. 3D surface averaging. To determine the discrepancy between two surfaces in the same stereotaxic system, a mesh construction algorithm generates a structured pattern of sample points at corresponding positions on surfaces outlined in different specimens, prior to examining the distances between the sets of corresponding points (Sclaroff and Pentland, 1994). Since the resolution of the meshes is standardized, the averaging of the 3D position vectors of corresponding nodes on meshes from each specimen yields an average surface representation for each sulcus.

points on the sulcus, and a corresponding set of $I \times J$ $100(1 - \alpha)\%$ confidence regions for any user-defined confidence threshold α . In addition, for each sulcus, a probability metric exists, namely,

$$\alpha_{\mathcal{F}}[\mathbf{r}^*(u, v)] = \sup \{ \alpha \mid \chi^2_{3df}(\alpha) \geq [\Delta^*(u, v)]^T [\Psi_{\mathcal{F}}(u, v)]^{-1} [\Delta^*(u, v)] \}, \quad \forall (u, v) \in \Omega.$$

This metric can be used to quantify the severity of local discrepancies $\Delta^*(u, v)$ between sulcal points $\mathbf{r}^*(u, v)$ in a new individual and the average representation of that sulcus.

Now we consider a complete set of disjoint or connected anatomic surfaces in the brain, delineated in a large number of brains in the same stereotaxic space and converted into parametric mesh form. For the same system of surface anatomy in a new subject, the degree of its local deviation from the average system of anatomic surfaces can be quantified locally. The result can be readily displayed, as a densely defined probability map, on a 3D surface representation of the individual's anatomy. To achieve this, we represent the surface anatomy of the new subject by a connected system of parametric meshes $\mathbf{r}_i^*(u, v)$, for $i = 1$ to k . The probability of this configuration is then given by the map

$$\alpha_{\mathcal{F}_i}[\mathbf{r}_i^*(u, v)] = \sup \{ \alpha \mid \chi^2_{3df}(\alpha) \geq [\Delta_i^*(u, v)]^T [\Psi_{\mathcal{F}_i}(u, v)]^{-1} [\Delta_i^*(u, v)] \}, \quad \forall (u, v) \in \Omega,$$

indicated by arrows that originate at points defined by the mesh. The map shown displaces the average representation of the right cingulate sulcus onto the equivalent surface in a randomly selected brain. Notice that the mesh in this figure contains a reduced number of points for the convenience of illustration. The coronal plane through the anterior commissure ($y = 0$) divides the anatomical architecture into two regions which are subjected, by the Talairach transform, to different scaling transformations in the anterior–posterior direction. This aspect of the stereotaxic transform may explain why the directional bias of local anatomical variation differs considerably for sulcal points on either side of this coronal plane.

for each $i = 1$ to k .

In this equation, $\Delta_i^*(u, v) = (\mathbf{r}_i^*(u, v) - \mathbf{r}_{i\mathbf{u}}(u, v))$, and $\Psi_{\mathcal{F}_i}(u, v)$ is the local 3×3 covariance matrix at (u, v) for the displacement maps defined on members of \mathcal{F}_i . The displacement maps are themselves given by

$$\{\Delta_j(u, v)\}_{j=1 \text{ to } n} = \{\mathbf{r}_j(u, v) - \mathbf{r}_{j\mathbf{u}}(u, v)\}_{j=1 \text{ to } n}, \\ \forall (u, v) \in \Omega \text{ and } \forall \mathbf{r}_j \in \mathcal{F}.$$

This closed form expression for the probability measure $\alpha_{\mathcal{F}_i}[\mathbf{r}_i^*(u, v)]$, for each node $\mathbf{r}_i^*(u, v)$ in a system of connected meshes, is conveniently evaluated. The range of the resulting probability values was mapped, via a logarithmic look-up table, onto a standard color range. Probability maps were visualized (using Data Explorer 2.1, IBM visualization software) by adding a range of colors to the surface representation of each sulcus. All 3D reconstruction programs were written in C and executed on DEC Alpha AXP3000 workstations running OSF-1.

RESULTS

Probability maps were created which highlighted abnormal deviations in the surface anatomy of a new subject. The medical history of the subject in question indicated the presence of lung cancer, which had spread to the brain. Two metastatic tumors were present, one in each hemisphere. The first, and larger, tumor (volume: 95.2 cm³; see Fig. 7a) was centered in the high putamen of the right hemisphere, 22.0 mm right of midline at the stereotaxic position (+7.5, +18.0, +22.0). A second tumor (volume: 24.6 cm³) was located in the left occipital lobe, lateral to the point of confluence of the parieto-occipital and calcarine sulci, with center 21.5 mm left of midline at (-64.0, +2.0, -21.5). The equivalent spherical diameters of the two tumors were 26.5 and 17.0 mm, respectively. No other neuropathology was present, and the primary cause of death was cardiopulmonary arrest. The subject's cognitive status was normal, although the tumor in the high putamen of the right hemisphere had resulted in contralateral hemiparesis. The positions of the tumor boundaries were, in each case, well-defined and did not compromise the structural integrity of the sulci.

The two regions of metastatic tissue induced marked distortions in the normal architecture of the brain. This effect was reflected both in the blockface imagery itself (Fig. 7a) and in the values of the probability maps of structures proximal to the lesion sites (Figs. 7b and 8). Examination of these probability maps reveals two general trends.

First, probability values were severely depressed for regions of structures proximal to the lesion sites. The body of the right callosal sulcus was shifted medially and vertically away from the tumor site, with 23.8% of its surface area having a probability value lower than

0.01. This value compared with a somewhat higher value of 27.5% for the right cingulate sulcus and values of 0.6, 0.0, and 0.0% for the parieto-occipital, anterior, and posterior calcarine sulci in the same hemisphere. Calculation of confidence limits for each surface revealed that 2.2% of the right callosal and 2.1% of the right cingulate sulcus were sufficiently abnormal to fall outside the $P = 0.0001$, or 1 in 10000, confidence threshold. In the left hemisphere, the anterior branch of the calcarine sulcus appeared to exhibit more severe deviations than the posterior branch (14.5 and 1.6% of their surface areas, respectively, have $P < 0.01$). The parieto-occipital sulcus, which was farther away from the lesion site, was not apparently affected (0.0% of its surface has $P < 0.01$).

Second, in the case of the abnormal subject, the extent to which the mechanical effects of the neoplasms propagated across the interhemispheric vault was quantified and highlighted by the probability maps (Figs. 7b and 8). Contralateral to the main lesion site, 5.7% of the left callosal and 4.3% of the left cingulate sulci (Fig. 7b) exhibited probability values depressed below the $P = 0.01$ threshold, with 0.1 and 2.3% of their surface areas, respectively, having $P < 0.0001$. Conversely, 99.4, 100.0, and 100.0% of the occipital surfaces contralateral to the *smaller* lesion had normal probability values ($P > 0.05$). Consistent with these results, herniation was apparent in the image data (Fig. 7a) in the vicinity of the largest tumor only.

As expected, similar normal results were obtained for all surfaces ($P > 0.05$), when probability maps were generated for each of the six normal subjects which made up the underlying database. In these cases, the anatomy of each normal subject was analyzed with respect to a database of sulcal surfaces from the five remaining subjects, with the local density functions being modified accordingly.

DISCUSSION

The surface decomposition and probabilistic mapping approaches developed here provide a framework for structural analysis of the interior surface anatomy of the brain in three dimensions. A family of surface maps was constructed, encoding statistical properties of local anatomical deviation within individual sulci. This process resulted in a probabilistic representation of sulcal anatomy, and enabled the automatic quantification and mapping of distributed patterns of abnormality in the anatomy of new subjects.

Cryosection Imaging

As an overall strategy for quantifying differences in the neuroanatomy of human subjects, an approach based on cryosectioning, in conjunction with high-resolution digital imaging of the specimen, presents

certain specific benefits and disadvantages. Several of these factors deserve to be emphasized. First, the composition of the sample group in this study was inevitably constrained by the inherent difficulties in acquiring high-quality, anatomic specimens from normal individuals via a Willed Body Program. Nevertheless, strict exclusion criteria were applied to guarantee, as far as possible, the selection of normal brains. No significant quantitative differences have been found between formalin-treated and untreated specimens, for a comprehensive range of spatial and geometric parameters (structural surface area, extent in three directions, curvature indices, and fractal dimension (Thompson *et al.*, 1995, 1996)). Recent investigations have involved the cryosectioning of human head specimens from individuals whose premortem and postmortem MR scans are available (Mega *et al.*, 1995). These studies have largely validated and underscored the potential of cryosectioning imaging as a spatially accurate, anatomic reference for brain mapping (Toga *et al.*, 1996).

In spite of the logistic difficulties, cryosectioning procedures present a number of highly advantageous features not available in the clinical imaging modalities. Cryosectioning techniques can be combined with a wide variety of molecular and neurochemical techniques on harvested tissue sections to enable parallel or subsequent characterization of regional anatomy at a very fine structural level. Comprehensive studies have revealed striking intersubject and interhemispheric variations in the distributions of primary neocortical fields and have clarified their relation to sulcal anatomy (Rademacher *et al.*, 1993). Accordingly, high-resolution images of cryosectioned human anatomy not only provide the necessary spatial and densitometric resolution for accurate morphometry, but also enable parallel or subsequent analysis of cellular fields and their molecular composition.

Probabilistic Brain Atlases

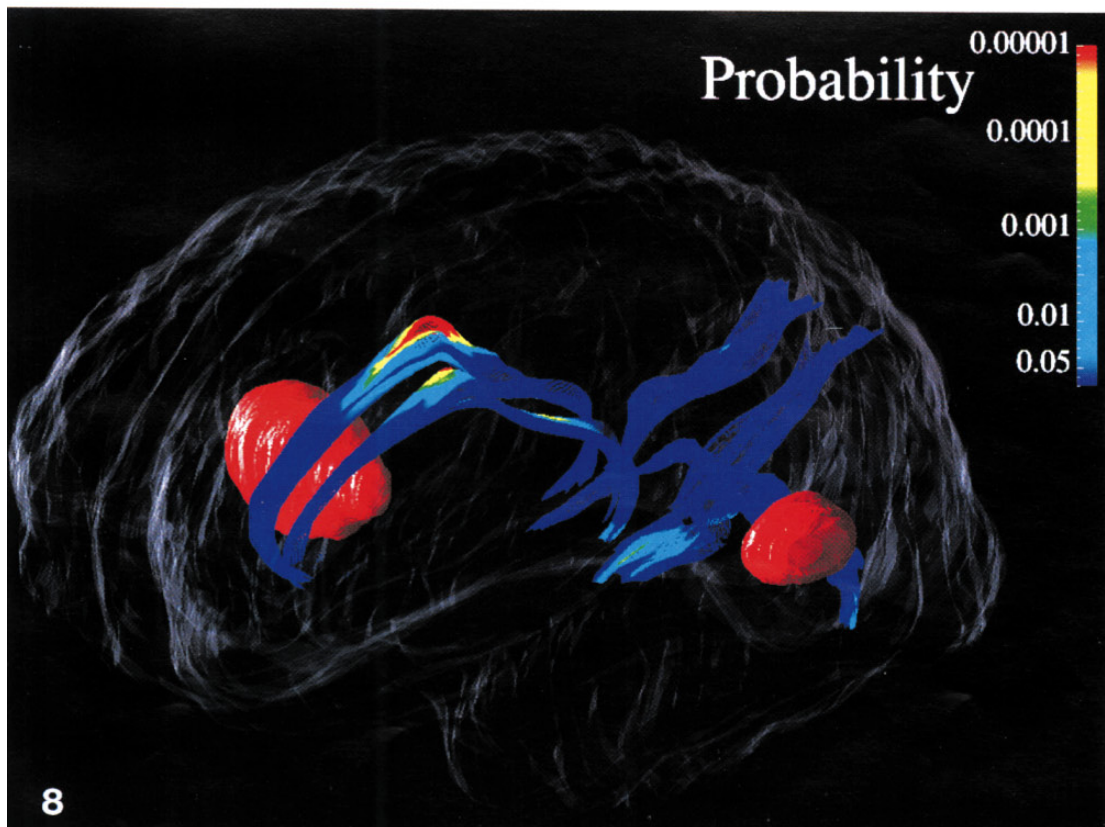
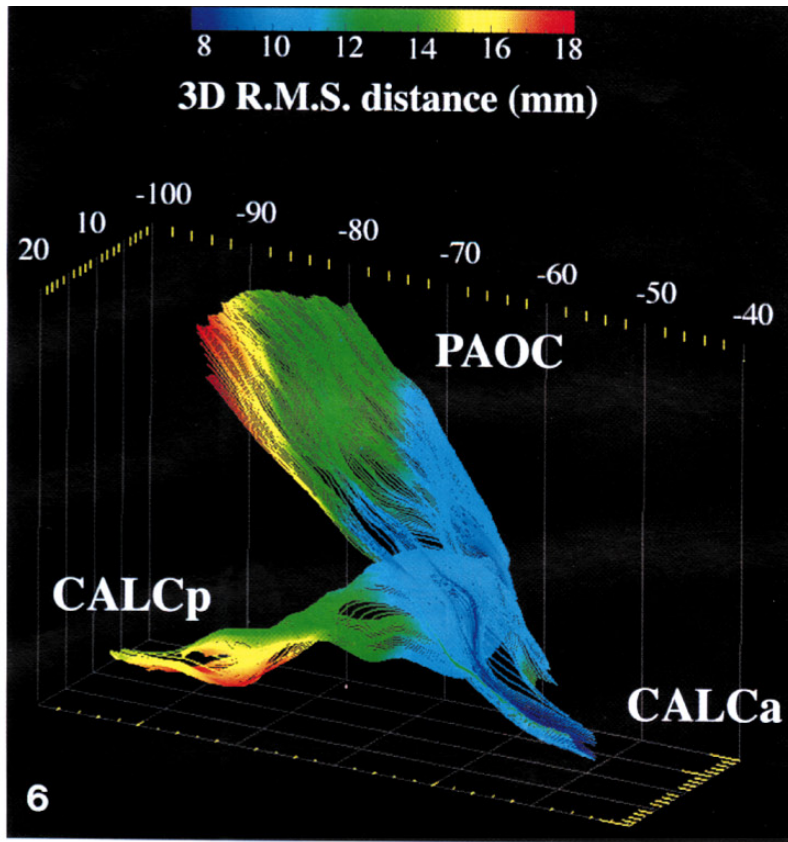
Methods for creating probabilistic representations of brain architecture currently fall into three major categories, each differing slightly in its conceptual foundations. In the voxel-based approach, large ensembles of

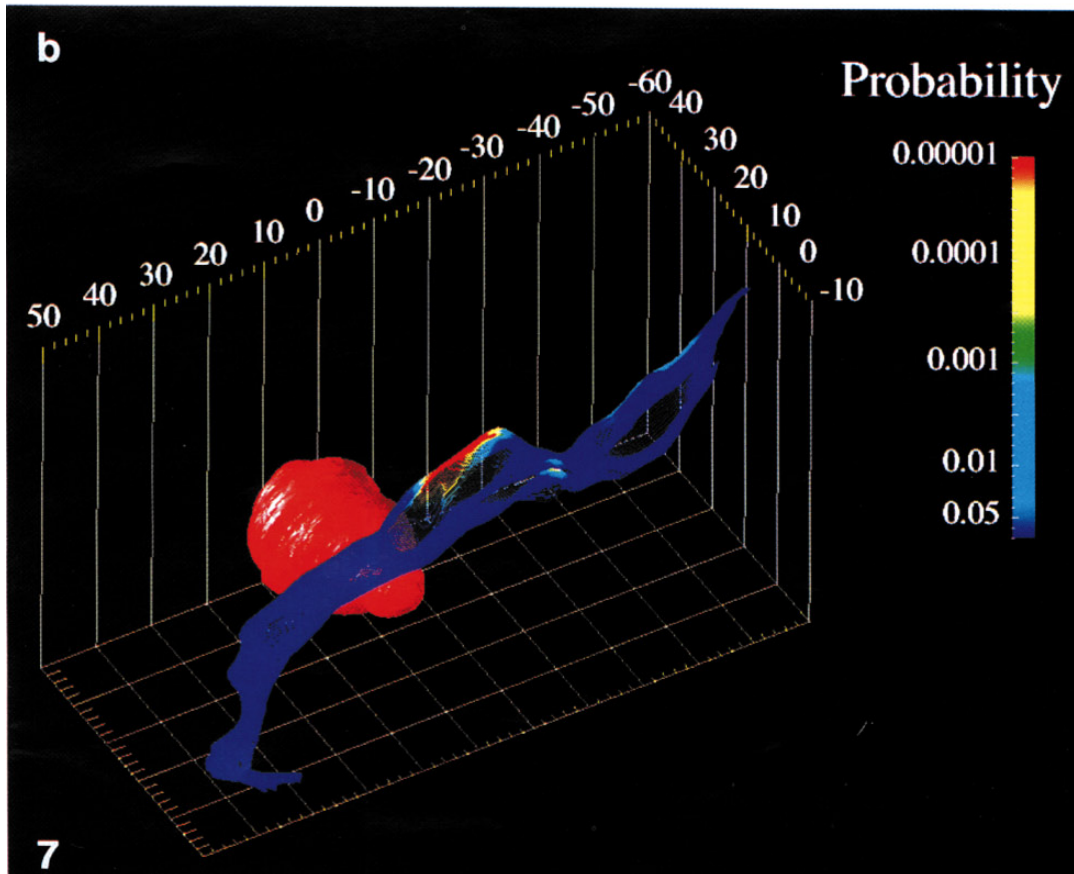
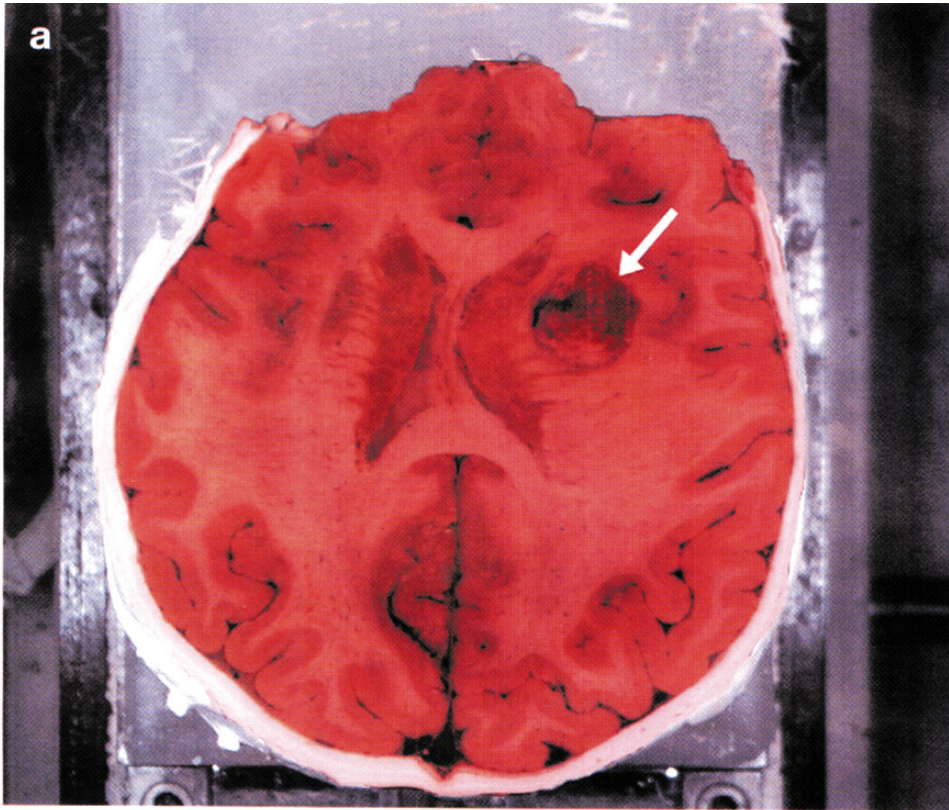
brain data are segmented into subvolumes, after mapping into stereotaxic space. A probability map can then be constructed for each tissue type, by determining the proportion of subjects assigned a given tissue label at each voxel (Evans *et al.*, 1994b; Otaky *et al.*, 1995; Paus *et al.*, 1996). In a second, density-based approach (Evans *et al.*, 1992), a large number of MRI scans are each intensity-normalized and averaged on a voxel-by-voxel basis, producing an average intensity MRI dataset. Finally, in the surface-based approach presented here, systems of connected parametric meshes model critical functional interfaces which form a natural partition of the brain's cellular architecture. For surface points in the anatomy of new subjects, algorithms defined on the database of anatomic data produce probability distributions and confidence limits for structure identification. Deviations in the anatomy of new subjects can therefore be analyzed and quantified at an extremely local level. Regardless of the modality of the source data, this procedure permits a high-dimensional estimation of the variability in normal brain architecture, incorporating information on its local directional biases. Recent investigations have revealed surprising directional trends in the patterns of normal anatomic variability (Thompson *et al.*, 1995, 1996). Anisotropic random fields, which are invoked in the generation of probability maps for new subjects, readily encode these subtle directional biases and hence quantify the severity of anatomic deviations more effectively than simple distance-based descriptors.

The surface-based approach presented in this paper may offer distinct advantages over volume averaging for statistical atlas applications. Surface-based representations lend themselves readily to averaging and subsequent statistical characterization. More particularly though, the averaging procedure itself does not lead to the same type of degradation of structural geometry (and loss of fine anatomic features) as is often apparent in volume averaging approaches. In addition, the retention of an explicit surface topology after averaging is particularly advantageous for subsequent visualization. This feature of both the individual and the average representations of brain anatomy enables secondary regional information, including local probabil-

FIG. 6. Variability maps and average surface representations for major sulci of the occipital lobe. 3D modeling and surface reconstruction techniques allow visualization of sulcal topography and greatly enhance the ability to appreciate complex spatial relationships. 3D representations are shown for three average sulci from the right occipital lobe of the six specimen brains. This oblique right-hand side view illustrates the course of the parieto-occipital sulcus from its anteroventral junction with the medial surface of the calcarine sulcus, which it divides into anterior and posterior segments. The posterior calcarine sulcus is shown joining it inferiorly. In this case, local variability is shown in color, on an average representation of each sulcus in Talairach stereotaxic space. The color encodes the root mean square magnitude of the displacement vectors required to map the surfaces from each of the six specimens onto the average, according to standard parametric criteria. Notice the pronounced increase in variability toward the exterior occipital surface.

FIG. 8. Probability maps for major sulci in both hemispheres. Color-coded probability maps are illustrated here on 3D surface models of the supracallosal, parieto-occipital, and anterior and posterior calcarine sulci in both hemispheres. All structures, including the two tumor sites (illustrated in red), are displayed within the Talairach stereotaxic grid, in the context of a transparent surface-rendered model of the exterior cerebral cortex. Again, structures in the immediate vicinity of the lesion sites exhibit probability values which are three orders of magnitude lower than normal ($P < 0.0001$), while more distal regions of these structures are normal ($P > 0.05$). Such surface models can be rotated and magnified interactively by the viewer to enhance the appreciation of complex spatial relationships.





ity maps, to be overlaid and visualized on the underlying surface models (Sclaroff, 1991). Information about physiology, neurochemistry, and an infinite variety of relevant maps can potentially be layered onto the anatomic atlas and referenced using such a system. In the brain, such surface maps might include cytoarchitecture, chemoarchitecture, blood flow distributions, and metabolic rates.

In the future, probabilistic mapping is likely to be fundamental to multisubject atlas and many other brain mapping projects. Given the pronounced anatomic variability between individual human brains, any atlas or clinical diagnostic system based on the anatomy of a single subject cannot succeed fully. Digital, probabilistic atlases based on large populations will rectify many current atlas problems, since they retain quantitative information on the variability inherent in anatomic populations. Nevertheless, such systems should be thought of as an ever-evolving process, rather than a single solution (Mazziotta *et al.*, 1995). By its very nature, a probabilistic atlas improves in accuracy over time, achieving better statistics as more information is added. As the database of subjects increases in size and content, the digital, electronic form of the atlas will provide efficiency in statistical and computational comparisons between individuals or groups. In addition, the digital form of the source data enables the population on which probabilistic atlases are based to be stratified into subpopulations by age, gender, by stage of development or to represent different disease types.

The ultimate goal of brain mapping is to provide a framework for integrating functional and anatomical data across many subjects and modalities. This task requires precise quantitative knowledge of the variations in geometry and location of intracerebral structures and critical functional interfaces. The surface mapping and probabilistic techniques presented here provide a basis for the generation of anatomical templates and expert diagnostic systems which retain quantitative information on intersubject variations in brain architecture.

APPENDIX

Construction of Surface Meshes

Parametric approaches to representing and mapping neuroanatomic surfaces have been fundamental to sev-

eral recent advances in the notion of mapping the cerebral cortex. Mathematical and cytoarchitectural considerations suggest that parametric mapping of architectonic surfaces offers a powerful method for representing complex associations between subregions of surfaces with subtle differences in geometry. Cortical flattening algorithms, for example, are based on an explicit parameterization of the cortical surface (Van Essen and Maunsell, 1980). Furthermore, parametric mesh approaches, which define a mapping of a 2D regular grid onto a complex 3D surface (Pedersen, 1994), have been validated as a paradigm for analysis of the cortical surface (MacDonald *et al.*, 1993; Evans *et al.*, 1994a). They have also formed the basis of boundary-based warping algorithms which integrate neuroanatomic data from subjects with different brain geometry (Ruprecht *et al.*, 1995). In particular, the explicit geometry provided by this approach allows convenient derivation of morphometric statistics, as well as quantitative indices of surface curvature, extent, area, fractal dimension, and geometric complexity.

Strategies for creating a regular parametric mesh from a stack of sulcal outlines contoured in a series of sagittal sections are analogous to stretching a regular rectangular grid, of size $I \times J$ (for any integers I and J), over all the scattered 3D point data digitized when outlining the sulcus. The mesh of grid points which results is parametric in the sense that its nodes can be indexed using the coordinates of the superimposed grid, u and v , (where u , and v are nonnegative integers). u and v are then said to be parametric coordinates for points on the surface. Three-dimensional surface points are given as position vectors in Talairach space by the function $\mathbf{r}(u,v) = (x(u,v), y(u,v), z(u,v))$. Step size in parameter space is quantized so that $\mathbf{r}(u,v)$ is really only defined for discrete (integer) values of u and v . $\mathbf{r}(u,v)$ can therefore be thought of as a polygonally defined surface of high resolution, determined by its vertices' locations (Lifshitz *et al.*, 1994). Due to the laminar topology of each sulcal surface S , the outlining procedure generates a set of parallel cross-sections $C_0, C_1, C_2, \dots, C_K$ of S , at $z_0, z_1, z_2, \dots, z_K$, where z is the lateral axis of Talairach space. Each contour is itself a set of 3D digitized points $C_k = \{P_i(x_i^k, y_i^k, z_i^k) \mid 0 \leq i \leq N_k\}$, where the number of points in each contour, N_k , varies for different contours, C_k , in the stack.

Step 1: To generate a mesh of size $I \times J$, we first divide each contour line into $I + 1$ points separated by a spacing of uniform length. For each C_k , let the cumu-

FIG. 7. Distortions in the architecture of the brain induced by tumor tissue. (a). Cryosection imagery. Color imagery taken from the blockface (here oriented at a caudal-to-rostral angle of depression of 27° , relative to the horizontal plane of Talairach space) reveals a well-defined metastatic lesion in the high putamen of the right hemisphere. Mechanical effects of the tumor tissue clearly propagate across the interhemispheric tissue (cf. (b)). (b). This oblique-angle view (from the perspective of the right eye orbit) illustrates the impact of the same tumor on the cingulate sulcus in the opposite hemisphere. Probability values are severely depressed ($P < 0.0001$; red colors) for regions of the cingulate sulcus proximal to the lesion site, although more distal regions of the same sulcus are normal ($P < 0.05$; deep blue colors). The severity of structural hemiation, due to the mechanical effects of a lesion, may therefore highlighted and quantified by probability mapping of structures in the opposite hemisphere.

lative are length $l(\mathbf{p}_i^k)$ to point $\mathbf{p}_i^k = P_i(x_i^k, y_i^k, z_i^k)$ be given by $l(\mathbf{p}_i^k) = \sum_{i=1}^k \|\mathbf{p}_i^k - \mathbf{p}_{i-1}^k\|$, where $\|\cdot\|$ is the classical Euclidean distance in 3D.

For each integer $u = 0$ to I , let $i(u) = \min\{i \mid l(\mathbf{p}_i^k) > u \cdot l(\mathbf{p}_{Nk}^k)/I\}$. For each value of u , we redigitize a point

$$\mathbf{q}_u^k = \mathbf{p}_{i(u)-1}^k + \lambda(\mathbf{p}_{i(u)}^k - \mathbf{p}_{i(u)-1}^k),$$

where $\lambda = \{(u \cdot l(\mathbf{p}_{Nk}^k)/I) - l(\mathbf{p}_{i(u)}^k)\} / \{l(\mathbf{p}_{i(u)}^k) - l(\mathbf{p}_{i(u)-1}^k)\}$. In the notation of (Chen *et al.*, 1990), this generates a family of parametric curves, given by

$$D^k = \{(u, k) \mid \omega(x_u^k, y_u^k, z_u^k) = (u, k), 0 \leq u \leq I, 0 \leq k \leq K\}.$$

Here u and k are two integer-valued parameters, and ω is a mapping which assigns coordinates (u, k) to the new vertex $\mathbf{q}_u^k = (x_u^k, y_u^k, z_u^k)$ of a redigitized contour.

Step 2: Step 1 yields a contour stack which is, as yet, only parametric in the sagittal plane. For a fully parametric mesh of size $I \times J$, we use a variant of Step 1 to produce an ordered set of $J + 1$ parametric curves, M^j , where the nodes of the final mesh are given by

$$M^j = \{(u, v) \mid \omega'(x_u^v, y_u^v, z_u^v) = (u, v), 0 \leq u \leq I, 0 \leq v \leq J\}$$

As before, ω' is a mapping assigning grid coordinates (u, v) to a nodal point $\mathbf{r}(u, v) = (x_u^v, y_u^v, z_u^v)$ in the mesh. Let \mathbf{q}_u^k be the point in D^k for which $\omega(x_u^k, y_u^k, z_u^k) = (u, k)$. Also let $l_u(\mathbf{q}_u^k)$ be the cumulative arc length $\sum_{i=1}^k \|\mathbf{q}_u^i - \mathbf{q}_u^{i-1}\|$. For each integer $v = 0$ to J , let $i(v) = \min\{i \mid l_u(\mathbf{q}_u^i) > v \cdot l_u(\mathbf{q}_u^J)/J\}$. For each value of v , we redigitize a point

$$\mathbf{r}(u, v) = \mathbf{q}_u^{i(v)-1} + \mu(\mathbf{q}_u^{i(v)} - \mathbf{q}_u^{i(v)-1}),$$

where $\mu = \{(v \cdot l_u(\mathbf{q}_u^J)/J) - l_u(\mathbf{q}_u^{i(v)})\} / \{l_u(\mathbf{q}_u^{i(v)}) - l_u(\mathbf{q}_u^{i(v)-1})\}$. The resulting set $\{\mathbf{r}(u, v) \mid 0 \leq u \leq I, 0 \leq v \leq J\}$ specifies the nodes of a regular parametric mesh of size $I \times J$ spanning the sulcal surface S .

Finally, when mapping a parametric grid from one sulcal surface, $\mathbf{r}^{(1)}(u, v)$, to another, $\mathbf{r}^{(2)}(u, v)$, the local internal stretching or contraction of the grid is represented by the continuous function

$$\theta(u, v) = \frac{\|\partial \mathbf{r}^{(2)}(u, v) / \partial u\| \cdot \|\partial \mathbf{r}^{(2)}(u, v) / \partial v\|}{\|\partial \mathbf{r}^{(1)}(u, v) / \partial u\| \cdot \|\partial \mathbf{r}^{(1)}(u, v) / \partial v\|}.$$

Consequently, the amount of local stretching which occurs when a parametric grid is mapped from one surface to another is unaffected by, and entirely independent of, any global translational or rotational shifts of one surface relative to the other.

Surface Mapping and 3D Distribution Theory

Let $\Omega = \{(u, v) \mid 0 \leq u \leq I, 0 \leq v \leq J; I, J, u, v \in \mathbb{N}\}$ be the lattice of integer-valued grid-points in a rectangular domain of \mathbb{R}^2 , with fixed size $I \times J$, (for any positive integers I and J). Let $\mathcal{F} = \{M_i, \Omega, n\}$ be the family of n parametric meshes $\mathbf{M}_i: \Omega \subset \mathbb{R}^2 \rightarrow \mathbb{R}^3$ defined on the same regular grid Ω (Fig. 3). These meshes may represent a given sulcus in n separate individuals, drawn from a specific population.

Second, we recall that an n -dimensional random variable \mathbf{X} with mean vector $\boldsymbol{\mu}$ and covariance matrix Ψ is said to have a nonsingular multivariate normal distribution, in symbols $\mathbf{X} \sim N_n(\boldsymbol{\mu}, \Psi)$, if (i) Ψ is positive definite and (ii) the probability density function of \mathbf{X} is of the form

$$f(\mathbf{x}; \boldsymbol{\mu}; \Psi) = \frac{1}{(2\pi)^{n/2} |\Psi|^{1/2}} e^{-[\mathbf{Q}_n(\mathbf{x}; \boldsymbol{\mu}; \Psi)]/2}, \quad \mathbf{x} \in \mathbb{R}^n,$$

where the exponent contains the quadratic form $\mathbf{Q}_n(\mathbf{x}; \boldsymbol{\mu}; \Psi) = (\mathbf{x} - \boldsymbol{\mu})^T \Psi^{-1} (\mathbf{x} - \boldsymbol{\mu})$.

Consider a general mesh $= \{\mathbf{r}(u, v) \mid (u, v) \in \Omega\}$ selected from the same population as the meshes in the family \mathcal{F} . The discrepancy between the mesh \mathbf{M} and the average mesh $\mathbf{M}\mathbf{r}_\boldsymbol{\mu} = \{\mathbf{r}_\boldsymbol{\mu}(u, v) \mid (u, v) \in \Omega\}$ can be represented by the displacement map $\Delta(u, v) = (\mathbf{r}(u, v) - \mathbf{r}_\boldsymbol{\mu}(u, v))$, $\forall (u, v) \in \Omega$. In particular, for a fixed choice of (u, v) , $\mathbf{r}(u, v) \sim N_3(\mathbf{r}_\boldsymbol{\mu}(u, v), \Psi_{\mathcal{F}}(u, v))$. Here $\Psi_{\mathcal{F}}(u, v)$ is the 3×3 covariance matrix whose entries are given by

$$\sigma_{ij}^2(u, v) = \frac{1}{n} \sum_{k=1}^n |\pi_i(\mathbf{r}_k(u, v) - \mathbf{r}_\boldsymbol{\mu}(u, v)) \cdot \pi_j(\mathbf{r}_k(u, v) - \mathbf{r}_\boldsymbol{\mu}(u, v))|,$$

where $1 \leq i, j \leq 3$, and π_1, π_2, π_3 are orthogonal projections onto each of the three axes of stereotaxic space. For our experimental data, at all (u, v) and for all 10 sulcal families \mathcal{F} , $\sigma_{ij}^2(i \neq j) \ll \sigma_{11}^2, \sigma_{22}^2, \sigma_{33}^2$, although $\sigma_{ii}^2(i = j)$. We therefore let $\Psi_{\mathcal{F}}(u, v) = \mathbf{diag}\{\sigma_{11}^2(u, v), \sigma_{22}^2(u, v), \sigma_{33}^2(u, v)\}$, where the σ_{kk}^2 are the variances of the x, y , and z components of the n maps $\mathbf{d}_i(u, v)$, respectively. This multivariate estimation approach increases the fidelity of the local probability density functions, so that for $\Delta = (\Delta x, \Delta y, \Delta z)^T$, the resulting density is

$$p(\Delta) \cdot d\Delta =$$

$$\frac{1}{(2\pi)^{3/2} \prod_{k=1}^3 \sigma_{kk}(u, v)} e^{-(1/2) \left[\left(\frac{\Delta x}{\sigma_{11}} \right)^2 + \left(\frac{\Delta y}{\sigma_{22}} \right)^2 + \left(\frac{\Delta z}{\sigma_{33}} \right)^2 \right]} \cdot d\Delta, \quad \Delta \in \mathbb{R}^3$$

where $\Pi_{k=1 \text{ to } 3} \sigma_{kk}^2$ is the determinant of $\Psi_{\mathcal{F}}(u,v)$. This relation assigns a set of $I \times J$ different nodal probability density functions which encode the distribution of general meshes \mathbf{M} around the average representation \mathbf{M}_{μ} of each sulcus.

3D Confidence Limits for Surface Variability

Now let $\mathbf{B}(0;1)$ be the closed unit sphere in \mathbb{R}^3 . For a specific choice of (u,v) , consider the ellipsoid

$$\mathbf{E}(u,v) = \{(\mathbf{r}_{\mu}(u,v) + [\Psi_{\mathcal{F}}(u,v)]^{-1/2} \mathbf{p} \mid \forall \mathbf{p} \in \mathbf{B}(0;1)\}$$

and the set of concentric ellipsoids $\mathbf{E}_{\lambda}(u,v) = \{\mathbf{r}_{\mu}(u,v) + \lambda[\mathbf{e} - \mathbf{r}_{\mu}(u,v)] \mid \forall \mathbf{e} \in \mathbf{E}(u,v), \forall \lambda \in \mathbb{R}^+, \text{ which are nested around it. Note that the form of the ellipsoids is completely determined by the transformation matrix}$

$$[\Psi_{\mathcal{F}}(u,v)]^{-1/2} = \mathbf{diag}\{\sigma_{11}^{-1}(u,v), \sigma_{22}^{-1}(u,v), \sigma_{33}^{-1}(u,v)\}.$$

As candidate locations for a mesh point $\mathbf{r}^*(u,v)$ in a new individual, points on the surface of any given ellipsoid $\mathbf{E}_{\lambda}(u,v)$ are isodense with respect to the probability density function $p(\delta).d\delta$. In fact, the loci of points of constant density are, in general, ellipsoids for which the quantity $\lambda^2 = |[\Psi_{\mathcal{F}}(u,v)]^{-1/2} \Delta^*(u,v)|^2$ is constant (Duda and Hart, 1973; Schalkoff, 1992). The quantity λ is often called the Mahalanobis distance from $\mathbf{r}^*(u,v)$ to $\mathbf{r}_{\mu}(u,v)$. Thus, the contours of constant probability density for the point $\mathbf{r}^*(u,v)$ are ellipsoids of constant Mahalanobis distance to its estimated mean position $\mathbf{r}_{\mu}(u,v)$. We therefore require to find the probability $p_{\mathbf{M}^*}(u,v)$, for each node $\mathbf{r}^*(u,v)$ in the mesh \mathbf{M}^* , of a further mesh point $\mathbf{r}(u,v)$ lying in the region $\mathbb{R}^3 \setminus \mathbf{E}_{\lambda}(u,v)$, where $\lambda = |[\Psi_{\mathcal{F}}(u,v)]^{-1/2} \Delta^*(u,v)|$. Accordingly,

$$1 - p_{\mathbf{M}^*}(u,v) = \Pr\{\Delta \in \mathbf{E}_{\lambda}(u,v)\} = \frac{1}{(2\pi)^{3/2} \prod_{k=1}^3 \sigma_{kk}(u,v)} \cdot \int_{E_{\lambda}} e^{-(1/2) \left[\left(\frac{\Delta x}{\sigma_{11}} \right)^2 + \left(\frac{\Delta y}{\sigma_{22}} \right)^2 + \left(\frac{\Delta z}{\sigma_{33}} \right)^2 \right]} \cdot dx dy dz.$$

Applying the linear transformation $[\Psi_{\mathcal{F}}(u,v)]^{-1/2}$ to the domain of the integral, and changing to spherical polar coordinates to simplify the expression for the region's boundary, we obtain

$$1 - p_{\mathbf{M}^*}(u,v) = \frac{1}{(2\pi)^{3/2}} \cdot \int_{\phi=0}^{2\pi} \int_{\theta=0}^{\pi} \int_{\rho=0}^{\lambda} e^{-\frac{1}{2} \rho^2} \rho^2 \sin \theta \cdot d\rho d\theta d\phi,$$

where $\lambda = |[\Psi_{\mathcal{F}}(u,v)]^{-1/2} \Delta^*(u,v)|$. The linear transformation does not affect any of the distributional properties of $p(\Delta(u,v)).d(\Delta(u,v))$, since the class of multivariate normal density functions is closed under transformations of location and scaling (Tong, 1990; Anderson, 1984). In addition, since $\Delta(u,v) \sim N_3(0, \Psi_{\mathcal{F}}(u,v))$ with $\Psi_{\mathcal{F}}(u,v)$ diagonal, and since the Cartesian components of the transformed variate $\mathbf{z}^*(u,v) = [\Psi_{\mathcal{F}}(u,v)]^{-1/2} \Delta^*(u,v)$ are independently distributed according to $N_3(0,1)$, the quantity

$$\lambda^2 = [\mathbf{z}^*(u,v)]^T [\mathbf{z}^*(u,v)] = [\Delta^*(u,v)]^T [\Psi_{\mathcal{F}}(u,v)]^{-1} [\Delta^*(u,v)]$$

is a χ^2 -distributed variable with 3 degrees of freedom (Anderson, 1984). This fundamental fact provides the basis for setting up tests and computing confidence regions concerning local displacements $\Delta(u,v)$. If we let $\chi_{3df}^2(\alpha)$ be the critical value of χ_{3df}^2 such that $\Pr\{\chi_{3df}^2 \geq \chi_{3df}^2(\alpha)\} = \alpha$, then the 100(1 - α)% confidence region for the stereotaxic position of the surface node at (u,v) is given in implicit form by the equation

$$\Pr\{[\Delta^*(u,v)]^T [\Psi_{\mathcal{F}}(u,v)]^{-1} [\Delta^*(u,v)] \leq \chi_{3df}^2(\alpha)\} = 1 - \alpha.$$

In other words, in a randomly selected individual from the population being considered, the probability is (1 - α) that the sulcal point $\mathbf{r}(u,v)$ will fall inside the confidence ellipsoid

$$\mathbf{E}_{\lambda(\alpha)}(u,v), \quad \text{where } \lambda(\alpha) = [\chi_{3df}^2(\alpha)]^{1/2}.$$

The volume of these confidence ellipsoids supplies a measure of the population dispersion for different atomic points in stereotaxic space. Its value varies, depending on the location of the surface point whose spatial probability distribution is being determined. For the surface point $\mathbf{r}(u,v)$, the associated 100(1 - α)% confidence ellipsoid has volume $C(3)(\det[\Psi_{\mathcal{F}}(u,v)])^{-1/2} \{\chi_{3df}^2(\alpha)\}^{3/2}/3$, where $C(3)$ is $2\pi^{3/2}/\Gamma(3/2) = 4\pi$, the surface area of the unit sphere in \mathbb{R}^3 . Finally, the resulting probability metric, namely,

$$\alpha_{\mathcal{F}}[\mathbf{r}^*(u,v)] = \sup\{\alpha \mid \chi_{3df}^2(\alpha) \geq [\Delta^*(u,v)]^T [\Psi_{\mathcal{F}}(u,v)]^{-1} [\Delta^*(u,v)]\}, \quad \forall (u,v) \in \Omega,$$

can be used to quantify the severity of local discrepancies $\Delta^*(u,v)$ between sulcal points $\mathbf{r}^*(u,v)$ in a new individual and the average representation of that sulcus.

ACKNOWLEDGMENTS

This work was generously supported by a Fulbright Scholarship from the US-U.K. Fulbright Commission, London, by Grant G-1-00001 of the United States Information Agency, and by a Pre-

Doctoral Fellowship of the Howard Hughes Medical Institute (P.M.T.). Research support was provided by the National Science Foundation (BIR 93-22434), by the National Library of Medicine (LM/MH05639), by the NCCR (RR05956), and by the Human Brain Project, which is funded jointly by NIMH and NIDA (P20 MH/DA52176). Special thanks go to Andrew Lee for his help in preparing the figures for this paper.

REFERENCES

- Anderson, T. W. 1984. *An Introduction to Multivariate Statistical Analysis*. Wiley, New York.
- Andreasen, N. C., Arndt, S., Swayze, V., Cizadlo, T., Flaum, M., O'Leary, D., Ehrhardt, J. C., and Yuh, W. T. C. 1994. Thalamic abnormalities in schizophrenia visualized through magnetic resonance image averaging. *Science* **266**: 294–298.
- Bailey, P. and von Bonin, G. 1951. *The Isocortex of Man*. Urbana, Univ. of Illinois.
- Burzaco, J. 1985. Stereotaxic pallidotomy in extrapyramidal disorders. *Appl. Neurophysiol* **48**: 283–287.
- Chen, S.-Y., Lin, W.-C., Liang, C.-C., and Chen, C.-T. 1990. Improvement on dynamic elastic interpolation technique for reconstructing 3D objects from serial cross-sections. *Trans. Med. Imag.* **9**(1): 71–83.
- Duda, R. O. and Hart, P. E. 1973. *Pattern Classification and Scene Analysis*. Wiley, New York.
- Evans, A. C., Dai, W., Collins, L., Neelin, P., and Marrett, S. 1991. Warping of a computerized 3D atlas to match brain image volumes for quantitative neuroanatomical and functional analysis. *Proc. Int. Soc. Opt. Eng. (SPIE): Med. Imag.* **III**: 264–274.
- Evans, A. C., Collins, D. L., and Milner, B. 1992. An MRI-based stereotaxic brain atlas from 300 young normal subjects. In *Proceedings of the 22nd Symposium of the Society for Neuroscience*, Anaheim, 408.
- Evans, A. C., Collins, D. L., Neelin, P., MacDonald, D., Kamber, M., and Marrett, T. S. 1994a. Three-dimensional correlative imaging: Applications in human brain mapping. In *Functional Neuroimaging: Technical Foundations* (R. W. Thatcher, M. Hallett, T. Zeffiro, J. E. Roy, and M. Huerta, Eds.), pp. 145–161. Academic Press, San Diego.
- Evans, A. C., Kamber, M., Collins, D. L., and MacDonald, D. 1994b. An MRI-based probabilistic atlas of neuroanatomy. In *Magnetic Resonance Scanning and Epilepsy* (S. D. Shorvon *et al.*, Eds.), pp. 263–274. Plenum, New York.
- Evans, A. C., Collins, D. L., and Holmes, C. J. 1996. Computational approaches to quantifying human neuroanatomic variability. In *Brain Mapping: The Methods* (A. W. Toga and J. C. Mazziotta, Eds.). Academic Press, in press.
- Hardy, T. L. 1994. Computerized atlas for functional stereotaxis, robotics and radiosurgery. *Proc. IEEE Conf. Vis. Biomed. Comput.* **2359**: 447–456.
- Lifshitz, L. M., Collins, J. A., Moore, E. D., and Gauch, J. 1994. Computer vision and graphics in fluorescence microscopy. In *Proc. of the IEEE Workshop on Biomedical Image Analysis, 24–25 June 1994*, pp. 166–175. IEEE Comput. Soc. Press, Los Alamitos, CA.
- MacDonald, D., Avis, D., and Evans, A. C. 1993. *Automatic Parameterization of Human Cortical Surfaces*. Annual Symp. Info. Proc. Med. Imag., (IPMI).
- Martin, J., Pentland, A., and Kikinis, R. 1994. Shape analysis of brain structures using physical and experimental models. In *Proc. of the IEEE Comput. Soc. Conference on Computer Vision and Pattern Recognition, 21–23 June 1994*. IEEE Comput. Soc. Press, Los Alamitos, CA.
- Mazziotta, J. C., Toga, A. W., Evans, A. C., Fox, P., and Lancaster, J. 1995. A probabilistic atlas of the human brain: Theory and rationale for its development. *NeuroImage* **2**: 89–101.
- Mega, M. S., Karaca, T. J., Pouratain, N., Chen, S., Adamson, C. F., Schluender, S., and Toga, A. W. 1995. Premortem–postmortem neuroimaging: A study of brain morphometric changes in man with MRI and cryomacrotome imaging. *Soc. Neurosci. Abstracts* **21**(1): 154.
- Miller, M. I., Christensen, G. E., Amit, Y., and Grenander, U. 1993. A mathematical textbook of deformable neuroanatomies. *Proc. Natl. Acad. Sci. USA* **90**: 11944–11948.
- Otaky, N., Paus, T., D'Avirro, D., Gutmans, D., MacDonald, D., Carmanos, Z., Tomaiuolo, F., and Evans, A. C. 1995. Volumetric Analysis of the Human Cingulate, Paracingulate, and Superior Rostral Sulci. *Soc. Neurosci. Abstracts* **21**(1): 154.
- Paus, T., Tomaiuolo, F., Otaky, N., MacDonald, D., Petrides, M., Atlas, J., Morris, R., and Evans, A. C. 1996. Human Cingulate and Paracingulate Sulci: Pattern, Variability, Asymmetry and Probabilistic Map. *Cerebral Cortex*, in press.
- Pedersen, H. K. 1994. Displacement mapping using flow fields. In *Proceedings of the SIGGRAPH Computer Graphics Conference*, pp. 279–286.
- Quinn, B., Ambach, K., and Toga, A. W. 1993. Towards a digital reconstruction human brain atlas. *Soc. Neurosci. Abstracts* **18**: 968.
- Caviness, V. S. Jr., Rademacher, J., Steinmetz, H., and Galaburda, A. M. 1993. Topographical variation of the human primary cortices: Implications for neuroimaging, brain mapping and neurobiology. *Cerebral Cortex* **3**(4): 313–329.
- Ruprecht, D., Nagel, R., and Muller, H. 1995. Spatial free-form deformation with scattered data interpolation methods. *Computers Graphics* **19**(1): 63–71.
- Sanides, F. 1962. Die Architektonik des menschlichen Stirnhirns. In (M. Mueller, H. Spatz, and P. Vogel, Eds.), Vol. 98, Monographien aus dem Gesamtgebiete der Neurologie und Psychiatrie. Springer-Verlag, Berlin.
- Schalkoff, R. J. 1992. *Pattern Recognition: Statistical, Structural and Neural Approaches*. Wiley, New York.
- Scaroff, S. 1991. *Deformable Solids and Displacement Maps: A Multi-Scale Technique for Model Recovery and Recognition*. Master's Thesis, MIT Media Laboratory, June 1991.
- Scaroff, S. and Pentland, A. 1994. On Modal Modeling for Medical Images: Underconstrained Shape Description and Data Compression. In *Proc. of the IEEE Workshop on Biomedical Image Analysis, 24–25 June 1994*, pp. 70–79. IEEE Comput. Soc. Press, Los Alamitos, CA.
- Steinmetz, H., Furst, G., and Freund, H.-J. 1989. Cerebral cortical localization: Application and validation of the proportional grid system in MR imaging. *J. Comp. Assist. Tomogr.* **13**(1): 10–19.
- Steinmetz, H., Furst, G., and Freund, H.-J. 1990. Variation of perisylvian and calcarine anatomic landmarks within stereotaxic proportional coordinates. *Am. J. Neuroradiol.* **11**(6): 1123–1130.
- Talairach, J., Szikla, G., Tournoux, P., *et al.* 1967. *Atlas d'anatomie stereotaxique du telencephalte*. Masson, Paris.
- Thompson, P. M., Schwartz, C., Lin, R. T., Khan, A. A., Toga, A. W., and Collins, R. C. 1995. 3D statistical analysis of sulcal variability in the human brain using high-resolution cryosection images. *Soc. Neurosci. Abstracts* **21**(1): 154.
- Thompson, P. M., Schwartz, C., Lin, R. T., Khan, A. A., and Toga, A. W. 1996. *3D Statistical Analysis of Sulcal Variability in the Human Brain*, submitted for publication.
- Toga, A. W., Ambach, K. L., Quinn, B., Hutchin, M., and Burton, J. S. 1994a. Post mortem anatomy from cryosectioned human brain. *J. Neurosci. Methods* **54**: 239–252.
- Toga, A. W., Ambach, K. L., and Schluender, S. 1994b. High-

- resolution anatomy from *in situ* human brain. *NeuroImage* **1**: 334–344.
- Toga, A. W., Ambach, K. L., Quinn, B., Shankar, K., and Schluender, S. 1995. Post mortem anatomy. In *Brain Mapping: The Methods* (A. W. Toga and J. C. Mazziotta, Eds.), Chap. 7, Academic Press, San Diego.
- Toga, A. W., Ambach, K. L., Quinn, B., Payne, B. A., Chao, K., and Yao, P. 1996. *Post Mortem Cross-Sectioning as an Anatomic Reference for Human Brain Mapping*, submitted for publication.
- Tong, Y. L. 1990. *The Multivariate Normal Distribution*. Springer-Verlag, New York.
- Van Essen, D. C. and Maunsell, J. H. R. 1980. Two-dimensional maps of the cerebral cortex. *J. Comp. Neurol.* **191**: 225–281.
- Vannier, M. W., Brunsdon, B. S., Hildebolt, C. F., Falk, D., Cheverud, J. M., Figiel, G. S., Perman, W. H., Kohn, L. A., Robb, R. A., Yoffie, R. L., and Bresina, S. J. 1991. Brain surface cortical sulcal lengths: Quantification with three-dimensional MR imaging. *Radiology* **180**: 479–484.